Article

Structure, Dynamics, and Substrate Specificity of the OprO Porin from *Pseudomonas aeruginosa*

Niraj Modi,[1] Sonalli Ganguly,[2] Iván Bárcena-Uribarri,[2] Roland Benz,[2] Bert van den Berg,[3,*] and Ulrich Kleinekathöfer[1,*]

[1]Department of Physics and Earth Sciences and [2]Department of Life Sciences and Chemistry, Jacobs University Bremen, Bremen, Germany; and [3]Institute for Cell and Molecular Biosciences, The Medical School, Newcastle University, Newcastle upon Tyne, UK

ABSTRACT The outer membrane (OM) of Gram-negative bacteria functions as a selective permeability barrier between cell and environment. For nutrient acquisition, the OM contains a number of channels that mediate uptake of small molecules by diffusion. Many of these channels are specific, i.e., they prefer certain substrates over others. In electrophysiological experiments, the OM channels OprP and OprO from *Pseudomonas aeruginosa* show a specificity for phosphate and diphosphate, respectively. In this study we use x-ray crystallography, free-energy molecular dynamics (MD) simulations, and electrophysiology to uncover the atomic basis for the different substrate specificity of these highly similar channels. A structural analysis of OprP and OprO revealed two crucial differences in the central constriction region. In OprP there are two tyrosine residues, Y62 and Y114, whereas the corresponding residues in OprO are phenylalanine F62 and aspartate D114. To probe the importance of these two residues in generating the different substrate specificities, the double mutants were generated in silico and in vitro. Applied-field MD simulations and electrophysiological experiments demonstrated that the double mutations interchange the phosphate and diphosphate specificities of OprP and OprO. Our findings outline a possible strategy to rationally design channel specificity by modification of a small number of residues that may be applicable to other pores as well.

INTRODUCTION

The outer membrane (OM) of Gram-negative bacteria acts as a molecular sieve because of the presence of channel-forming proteins (1,2). These proteins form β-barrels in the OM and are responsible for the transport of hydrophilic solutes and nutrients across the OM. OM channels differ in their specificity with respect to the substrates that can permeate through them. Some are nonspecific (e.g., OmpF, OmpC) and allow general diffusion of hydrophilic molecules below a certain size (1,2) generally based on the size-exclusion principle, whereas others are responsible for the permeation of specific substrates such as carbohydrates (LamB and ScrY (3,4)), nucleosides (Tsx (5)), and phosphate ions (OprP (6,7)). Such substrate specificities are achieved by the virtue of having a defined substrate binding site in the channels. Understanding the specificity and transport properties of OM channels is an active area of research with implications ranging from nanoanalytics (e.g., nanopore-based DNA sequencing) (8–10) to research on how to improve antibiotic translocation through OM channels (11,12).

Pseudomonas aeruginosa (Pa) is an opportunistic Gram-negative pathogen and is a major cause for nosocomial infections. The OM of the Pa bacterium contains, as known so far, no classical porins but only narrow and substrate selective channels (e.g., channels of the OprD/Occ-family) and the lack of wide pores is likely the reason for the poor permeation of antibiotics through the Pa OM. Among these substrate-selective channels is OprP, a phosphate-selective porin that is induced under phosphate starvation conditions and facilitates the high-affinity acquisition of phosphate ions that are important for *Pseudomonas* growth and proliferation (7). A crystal structure of OprP is available (13) and detailed investigations have been carried out to understand the phosphate specificity of this interesting channel using bilayer electrophysiological measurements (6,14,15) and computational molecular dynamics (MD) simulations (16–19).

A homologous channel to OprP from Pa, OprO, shares a high sequence similarity and identity of 86% and 74%, respectively, with OprP (20,21). However, bilayer measurements have demonstrated that OprO is selective for polyphosphate, e.g., pyrophosphate whereas OprP is selective for phosphate (15,20). The difference in the specificity of highly similar channels is intriguing, and therefore we performed further structural and mechanistic investigations. The details gained from such experiments might have implications that are not limited to understanding the differences in the specificity between these two particular channels but could potentially provide a template to fine-tune the specificity and transport properties of various ion channels. The

Submitted April 21, 2015, and accepted for publication July 28, 2015.

*Correspondence: bert.van-den-berg@ncl.ac.uk or u.kleinekathoefer@jacobs-university.de

Niraj Modi and Sonalli Ganguly contributed equally to this work.

Editor: Bert de Groot.

0006-3495/15/10/1429/10

http://dx.doi.org/10.1016/j.bpj.2015.07.035

major bottleneck in such engineering efforts is the availability of a crystal structures for both channels. In this study we report the x-ray crystal structure of the Pa OprO channel. In addition, bilayer electrophysiological measurements and free-energy MD simulations have been carried out to understand the polyphosphate specificity of this pore. Going one step further, we show that with the help of mutagenesis studies one can interconvert the specificity of OprP and OprO. In particular we have theoretically and experimentally demonstrated that an engineered double mutant channel of OprP has OprO-like properties and becomes selective for pyrophosphate.

MATERIALS AND METHODS

Bacterial strains and growth conditions

Escherichia coli (*E. coli*) strain DH5α was used as a host for maintaining the clones containing the OprP expression plasmid pAS27 (22) and various other plasmid containing single and double mutants. For overexpression and purification of OprO wild-type, OprP wild-type and its mutant proteins, *E. coli* CE1248 cells were used (23). These cells lack major *E. coli* pore forming proteins such as OmpC, OmpF, and PhoE. *E. coli* CE1248 harboring these wild-type and mutant plasmids were cultured on Luria-Bertani (LB) agar (Roth, Germany) plates supplemented with 100 μg/ml ampicillin (Roth, Germany) for plasmid maintenance. Growth of the cells was maintained as described in the Supporting Material.

Preparation of pores for electrophysiology, sodium dodecyl sulfate-polyacrylamide gel electrophoresis, and Western immunoblotting

Cloning, site-directed mutagenesis, and sequencing of OprP wild-type and mutants are described together with the extraction and purification of OprP and OprO for electrophysiology experiments in the Supporting Material. Furthermore, sodium dodecyl sulfate-polyacrylamide gel electrophoresis (SDS-PAGE) and Western immunoblotting (WB) were performed as described in the Supporting Material.

Cloning, purification, and crystallization of OprO

The mature part of Pseudomonas PAO1 *oprO* was amplified from genomic DNA by polymerase chain reaction, digested with XhoI/XbaI, and cloned into the arabinose-inducible pB22 vector. The resulting construct has the signal sequence from *E. coli* TamA, and OprO is fused at the N-terminus with a heptahistidine tag. After signal peptidase cleavage the N-terminal sequence of the protein is as follows: ANVRLQHHHHHHHLE-OprO. Protein expression was performed using C43 ΔcyoABC*D* cells by growing the cells at 37°C until optical density (OD) 0.5–0.7, followed by induction for 16 h at 20°C using 0.1% (w/v) arabinose. Cells were resuspended in buffer A (20 mM Tris/300 mM NaCl pH 8) and broken via one pass through a cell disrupter (Constant Systems, Daventry, UK) at 23 kpsi. Total membranes were collected via ultracentrifugation (Beckman (Brea, CA) L8-80 ultracentrifuge) for 45 min at 45 krpm using a 45 Ti rotor (Beckman). The membranes from 12 liter cells (OD600 ~1–1.5) were resuspended in 100 ml buffer A containing 2.5% Elugent (w/v; Calbiochem) followed by stirring at 4°C for 2 h. The suspension was centrifuged for 30 min at 45 krpm and the supernatant loaded onto a 10 ml nickel column equilibrated in buffer A + 0.2% (w/v) lauryldimethylamine N-oxide. Washing occurred with 150 ml buffer + 30 mM imidazole and the protein was eluted with 30 ml buffer + 250 mM imidazole. The protein was concentrated by ultrafiltration and loaded onto a Superdex-200 column equilibrated in 10 mM Hepes/100 mM NaCl/0.12% decyl-maltoside pH 7.5. For polishing and detergent exchange, a second gel filtration column was run in 10 mM Hepes/100 mM NaCl/0.3–0.4% C_8E_4 pH 7.5. For crystallization, the protein was concentrated by ultrafiltration (100 kDa cutoff) to ~10 to 15 mg/ml, aliquoted, and flash-frozen in liquid nitrogen.

Crystallization trials were performed by sitting drop vapor diffusion with commercial (MemGold 1 and 2, Morpheus; Molecular Dimensions (Suffolk, UK)) and in-house crystallization screens using a Mosquito crystallization robot (TTP Labtech, Melbourn, UK). Initial hits were optimized and scaled up using sitting and hanging drops. Wild-type OprO gave well-diffracting crystals in 10 mM sodium acetate/0.2 M ammonium sulfate/10-15% PEG4000 pH 4. Crystals of the OprO-to-P double mutant F62Y/D114Y were obtained in 50 mM sodium acetate/0.225 M ammonium sulfate/12% PEG 4000 pH 4.

Diffraction data were collected on beamline X6A of the National Synchrotron Light Source (NSLS) for wild-type OprO and on beamline i02 of the Diamond Light Source for the OprO-to-P mutant. Both proteins crystallized in space group R3, with cell dimensions of ~87 × 87 × 159 Å (angles 90° × 90° × 120°). In both cases the asymmetric unit contains one monomer, corresponding to a solvent content of ~50% (V_m = 2.5 $Å^3$/Da). The physiological trimer is generated by crystal symmetry operations. Diffraction data were processed with XDS (24). The OprO structure was solved by molecular replacement with Phaser (25), using OprP as the search model (PDB ID 2O4V (13)), and refined within Phenix (www.phenix-online.org) (26) with translation libration screw-motion restraints but without applying non-crystallographic symmetry restraints. The refined structure of OprO was used as the search model for the OprO-to-P mutant. The data collection and refinement statistics are summarized in Table S4.

Electrophysiology

The black lipid membrane assay has been previously described in detail (17). In brief: a membrane was formed from a 1% (w/v) solution of diphytanoylphoshatidylcholine (DiPhPC, Avanti Polar Lipids, Alabaster, AL) in n-decane (Fluka Sigma-Aldrich, Seelze, Germany) over a 0.4 mm^2 aperture, between two aqueous compartments in a Teflon cell. Two Ag/AgCl electrodes with salt bridges were inserted on both sides of the Teflon cell. One of the electrodes was connected via a voltage source to ground and the other electrode was connected to a current amplifier (Keithley 427) to measure the current passing through membrane and electrodes. The output signal of the amplifier was monitored with a digital oscilloscope and a strip-chart recorder (Rikadenki Electronics, Freiburg, Germany). Titration experiments were carried out to measure the inhibition of chloride conductance by phosphate binding to the binding sites, as previously described in detail with OprP wild-type and its mutants (16,17). Details are given in the Supporting Material.

Molecular dynamics simulations

The OprO and OprP proteins based on their crystal structures (PDB code 2O4V for OprP (13)) were embedded into a palmitoyloleoyl-glycero-phosphathidyl ethanolamine (POPE) lipid bilayer that was constructed from preequilibrated patches using VMD (27). Subsequently, the system was solvated using TIP3P water molecules. Either phosphate or diphosphate ions were subsequently placed at the mouth of the one of the monomers on the extracellular side for each porin. The monovalent form of the phosphate ion, $H_2PO_4^-$, was investigated consistent with our previous studies (16–18), whereas the divalent form of the diphosphate ion, $H_2P_2O_7^{2-}$ was chosen as the most probable protonation state at pH 6. The systems were neutralized by addition of potassium ions and each system contained roughly 120,000 atoms. For the mutant studies, the F62 and D114 residues of OprO were mutated to the corresponding residues of OprP, i.e., Y62 and Y114 and vice versa. The mutant systems were subjected to 5000 steps of

energy minimization to remove unfavorable steric contacts followed by 10 ns long equilibration runs.

The simulations were performed in the NPT ensemble with the program NAMD 2.8 (28) and the CHARMM27 force field (29) along with additional force field parameters for $H_2PO_4^-$ (30). Force field parameters for $H_2P_2O_7^{2-}$ were obtained with the help of the ParamChem web-server that performs an assignment of parameters and charges using analogy principles (31,32). The temperature of 310 K and the pressure of 1 atm were maintained in all the simulations using Langevin dynamics along with a Langevin piston algorithm. Moreover, periodic boundary conditions were used in the simulations. Short-range nonbonded interactions were calculated using a cutoff of 12 Å and a switching distance of 10 Å. The long-range electrostatic interactions were accounted for using the particle mesh Ewald (PME) method (33). Bonded interaction were evaluated every 1 fs. Moreover, short-range nonbonded and long-range electrostatic interactions were determined every 2 and 4 fs, respectively, using the r-RESPA multiple time step method (34). In addition, the SHAKE constraint algorithm was employed concerning the hydrogen bonds of all water molecules.

The adaptive biasing force (ABF) approach (35,36) as implemented in the collective variable module of the NAMD 2.9 program was applied to calculate the effective free energy profiles for the transport of different ions through OprP, OprO, and their mutants. The principal axis of the channel was always aligned parallel to the z axis and the reaction coordinate was assigned to be the z position of the ion. The change in free energy was determined with respect to the bulk value. The full reaction coordinate with a length of 84 Å along the z axis was subdivided into 21 windows with a length of 4 Å each to enhance the sampling efficiency. This range of the reaction coordinate along the z axis also consists of extended bulk regions on both sides of the channel. The initial starting conformations of the system for each window were retrieved by constant velocity steered molecular dynamics (SMD) simulations wherein each respective studied ion was dragged through the channel along the z axis. In the ABF method, the average force acting on the respective ion was accumulated in 0.1 Å sized bins within each window. In addition, the application of the adaptive bias was initiated only after 800 samples were accumulated in the individual bins to address the issue of the fluctuating instantaneous forces and to calculate a reasonable starting estimation of the biasing forces. Later on, the resulting data were integrated to generate the potential of mean force (PMF) profiles. Production runs in each window were carried out for at least 6 ns whereas considerably extended runs were performed for ~20 to 25 ns in the central binding site windows (−10 to 10 Å).

RESULTS AND DISCUSSION

Structure and dynamics of OprO

An interesting crystallographic detail in both OprO structures is that the N-terminal cloning region incorporating the His7 tag has a well-defined conformation and interacts with a neighboring trimer within the crystal (Fig. S1). It is not clear to what extent the tag contributes to the packing in the crystal, but it does show that the presence of a sizeable tag (15 residues) is not necessarily detrimental to obtaining well-ordered crystals. The crystal structure of OprO revealed its trimeric organization and each monomer is composed of 16 β-strands that are connected to each other via extracellular loops (L) and periplasmic turns (T). Loops L3, L5, and T7 fold inside the lumen of the pore and form narrow regions across the length of the pore lumen (Fig. 1). Because of the high sequence similarity with OprP, OprO shares many structural features with OprP as expected from a C_α r.m.s.d of 0.55 Å (411 atoms aligned). For example, OprO also contains the so-called arginine ladder where arginine residues (R219, R221, R243, R223, R227, R59, R60, and R34) span from the extracellular region to the center of the pore in a ladder-like fashion (Fig. 1). These arginine residues are believed to provide an electropositive sink to attract the phosphate ions from the dilute extracellular environment (13,18). Furthermore, on the periplasmic side of the channel, clusters of lysine residues (K30, K74, K15, 326, K109, and K126) are present as is also the case in OprP.

To further understand the structure and particularly the dynamics of OprO, we carried out unbiased MD simulations with OprO embedded in a membrane and compared it with the dynamics of OprP. Root mean square fluctuation analysis revealed that both channels, OprO and OprP, show

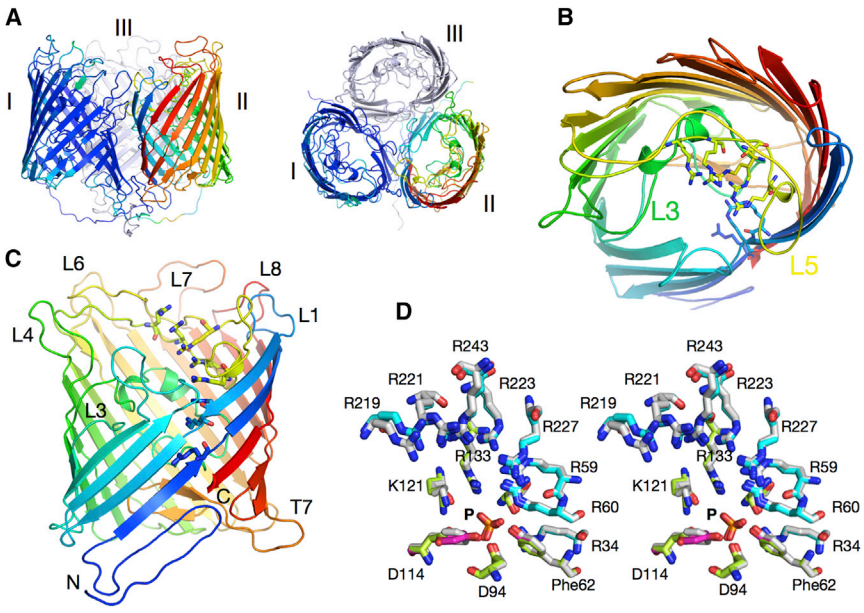

FIGURE 1 X-ray crystal structure of *Pseudomonas aeruginosa* OprO. (*A*) Overview of the trimer viewed from the side (*left*; extracellular side is up) and from the extracellular side. Monomer I is colored by B-factor: low (*blue*) and high (*red*). Monomer II is in rainbow representation with the N-terminus in blue. (*B*) Close-up cartoon of an OprO monomer from the extracellular side, showing the basic ladder residues as stick models. Extracellular loops L3 and L5, constricting the channel, are indicated. Loops have been smoothed for clarity. (*C*) Side view of the OprO monomer showing the basic ladder residues. (*D*) Stereo representation of superpositions of the basic ladder and phosphate (P) binding site residues for OprP (*gray*) and OprO (*cyan*, basic ladder residues; *green*, phosphate binding site residues). In addition the mutated side chains for the OprO to P mutant protein are shown in magenta (Y62 and Y114). The indicated numbering is that for OprO. To see this figure in color, go online.

similar fluctuations within the statistical error limits in unbiased MD simulations (Fig. 2 *C*). From 2500 snapshots of the unbiased MD simulations, average pore radii were determined for OprO and OprP using the program HOLE (Fig. 2, *A* and *B*). The most notable differences in radii were found at the central region of the pores, from −4 Å to 2 Å, where OprO has a higher average radius compared with OprP. The radius difference is because of different residues present in both channels across the lumen of the pore. Particularly significant are the residues D114 and F62 in the central region of OprO where the corresponding residues in OprP are bulkier and correspond to Y114 and Y62 (Fig. 2 *B*). Moreover, OprO shows larger fluctuations in the pore radius compared with OprP, as denoted by larger error bars especially around 0 Å, indicating that this region is more flexible in OprO. The dynamics of the channels can be determined by the network of salt bridges and H-bonds between the different residues of the channels. A salt bridge is present between the residues D145 and R182 in OprP throughout the complete unbiased MD simulation of 25 ns. The corresponding residues in OprO, i.e., T145 and Q183, cannot form salt bridges. In addition, in OprP the side chains of residues Y62 (F62 in case of OprO), Y79 (F79), Y183 (F184), T136 (A136), S166 (G167), and N382 (A385) have the ability to form H-bonds because of the presence of H-bond donor/acceptor groups, whereas the side chains of the corresponding residues in OprO as listed in parentheses lack this ability. These facts may explain the larger variances of the OprO pore radius in the central region compared with OprP. The larger pore radius of OprO relative to OprP is in agreement with the higher conductance observed with electrophysiology for OprO compared with OprP (Table 1) (6,21).

Diphosphate specificity of OprO versus phosphate specificity of OprP

Bilayer electrophysiological measurements suggest that diphosphate ions have a stronger binding affinity for OprO whereas phosphate ions bind more strongly to OprP (Table 1). Free-energy MD simulations were carried out to obtain the molecular details about the difference in the binding affinity of phosphate and diphosphate toward OprO and OprP. We already investigated the permeation of phosphate through OprP using free-energy MD simulations in a previous study (18).

The PMF profile for phosphate transport through OprO revealed two central phosphate binding sites (P1 and P2) with a well depth of ~7 kcal/mol (Fig. 3 *A*). These two binding sites are spatially separated by ~5 Å along the *z* axis with an energy barrier of roughly 2 kcal/mol between them. In terms of the overall shape, this PMF profile is very similar to phosphate transport through OprP (Fig. 3 *A*) (18). Such similar shapes of the profiles are not very surprising considering the fact that OprP and OprO share a very high sequence identity. Nevertheless, the major difference between the two channels in terms of phosphate transport is the depth of the binding sites for phosphate. Phosphate has a binding well depth of 7 kcal/mol in OprO compared with 9 kcal/mol in OprP (Fig. 2 *A*). The deeper potential

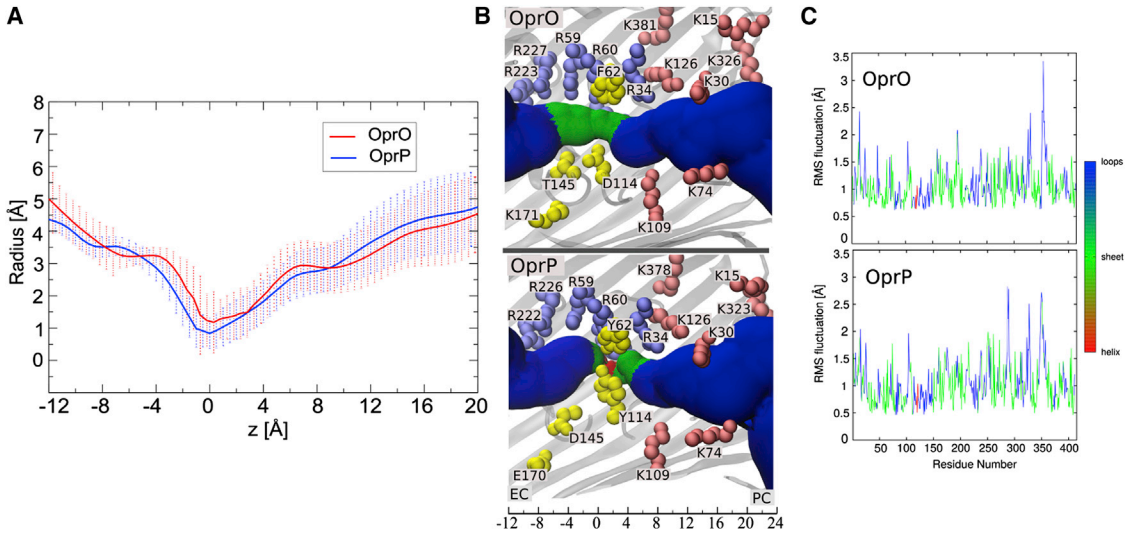

FIGURE 2 Structural features of OprO compared with OprP. (*A*) Average radius of the OprO and OprP channels along with the corresponding standard deviation derived from unbiased MD simulations. The pore radii have been determined using the HOLE program (47). (*B*) Structural features of OprO and OprP. Approximate relative radii of both pores are indicated by a solid-surface presentation. The different regions are color coded according to an average radius in the respective regions: radius above 3 Å (*blue*); between 1 to 3 Å (*green*); below 1 Å (*red*). Important residues along the ion permeation pathway are labeled and mapped to their position along the *z* axis. The yellow-colored residues are nonconserved between OprP and OprO and might be important for the different ion specificity of OprP and OprO. The other colored residues are preserved in OprP and OprO. (*C*) Root mean square fluctuations for OprO and OprP derived from unbiased MD simulations. To see this figure in color, go online.

TABLE 1 Single-channel conductance in 100 mM KCl and inhibition of chloride-mediated conductance by phosphate and diphosphate through OprO, OprP, and OprP mutant channels

		Phosphate		Diphosphate	
Porin	G(pS)	Half-Saturation Constant (mM)	Stability Constants (K in 1/M) for Inhibition	Half-Saturation C onstant (mM)	Stability Constants (K in 1/M) for Inhibition
OprO (wild-type)	240	4.5	220 ± 50	0.6	1450 ± 120
OprP (wild-type)	160	1.3	770 ± 150	3.2	310 ± 35
OprP (Y62F)	160	3.1	320 ± 40	1.7	590 ± 50
OprP (Y114D)	180	1.6	600 ± 75	3.0	330 ± 25
OprP (Y62F Y114D) (P→O)	240	8.3	120 ± 50	0.7	1260 ± 120

The single-channel conductance was measured in 0.1 M KCl, 10 mM MES, pH 6, T = 20°C, and applying 50 mV voltage. At least 100 single events were used to calculate the average value of conductance. The half-saturation and stability constants for inhibition of Cl^- conductance by phosphate or diphosphate were obtained from titration experiments using either the Michaelis-Menten equation or the Langmuir equation as described elsewhere (3,17). The phosphate and diphosphate solutions had a pH of 6. Mean values (± SD) of at least three individual titration experiments are shown.

well in OprP leads to a stronger binding of phosphate in OprP than in OprO and thus may contribute to the experimentally observed phosphate specificity of OprP. In OprO the binding site P1 is formed by residues R59, R60, K121, and R133 whereas the binding site P2 is formed by residues R34, F62 (Y62), D94, S124, S125, and R133 (Fig. 2 *C*). The same residues are involved in the formation of binding sites P1 and P2 for phosphate in OprP unless stated otherwise in parentheses.

For diphosphate transport through OprO there exist two central binding sites, D1 and D2, with an energy well-depth of ~9 kcal/mol (Fig. 3 *A*). D1 and D2 are separated by a barrier of 5 kcal/mol and are spatially 6 Å apart from each other. In the case of OprP, the overall PMF profile is quite similar to the one observed for OprO except for the fact that diphosphate experiences only one central binding site in OprP, i.e., D1, whereas site D2 is missing (Fig. 3 *A*). It may be concluded that the higher affinity of OprO for diphosphate is because of the presence of two central binding sites compared with only one site in OprP. Two defined central binding sites for diphosphate in OprO increase the overall pore attractive volume for diphosphate at the center

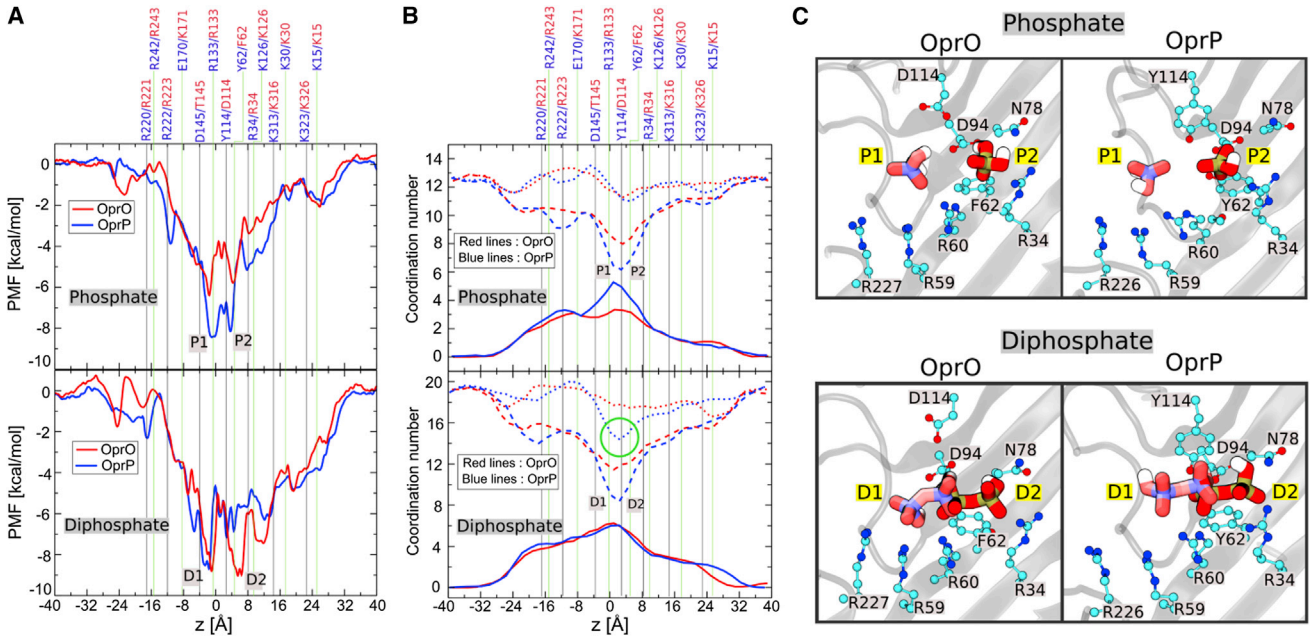

FIGURE 3 (*A*) PMF profiles for the transport of phosphate and diphosphate through OprO and OprP. Important residues of OprP and OprO along the ion permeation pathway are mapped onto the PMF profiles with respect to their positions along the *z* axis and labeled at the top of the figure: OprO (*red label*); and the corresponding residues in OprP (*blue labels*). (*B*) Coordination numbers, i.e., protein (*solid line*), water (*dash line*), and total (*dotted line*) contacts, for the permeation of phosphate and diphosphate through OpO (*red*) and OprP (*blue*). (*C*) Representative snapshots for phosphate in the binding sites P1 and P2 as well as for diphosphate in the binding site D1 and D2 of OprO and OprP. In OprP the diphosphate binding site D2 is absent; however, we have shown the diphosphate ion in OprP at the same position as that of the site D2 in OprO for comparison. Phosphate and diphosphate are shown using a stick representation whereas some of the interacting residues of the channels are shown using a ball and stick representation. Two phosphates or diphosphates are shown to demonstrate the relative positions of the binding sites though there is no experimental evidence for a double occupancy of the channel. The PMF calculations have been performed with phosphate or diphosphate ions. To see this figure in color, go online.

of the channel. The substrate may also hop from one site to the other, contributing to a stronger binding affinity of diphosphate for OprO compared with OprP. In OprO the binding site D1 is formed by the residues R59, R60, D94, D114 (Y114), K121, and R133 whereas the binding site D2 is formed by the residues R34, F62, N78, D94, D114, S124, S125, and R133 (Fig. 3 *C*). In OprP, binding site D1 is formed by the same residues as mentioned for OrpO unless stated otherwise in parentheses, whereas site D2 is absent.

We hypothesize that the specificity for phosphate or diphosphate of either OprP or OprO, can be a result of geometrical factors, such as a pore size, or of the different distributions of the charged amino acids between the two porins or a combination of both. From the geometrical point of view, the pore diameter averaged over the MD trajectory is smaller for OprP compared with OprO especially in the narrowest part of the pore (Fig. 2, *B* and *C*). The two bulky aromatic tyrosine residues (Y114 and Y62) in OprP constrict the narrowest part in the pore. At the same position, the pore diameter is larger for OprO because of the presence of less bulky residues, i.e., D114 and F62. From the charge distribution point of view, D114 in OprO is most likely important for the diphosphate specificity as the corresponding residue in OprP, Y114, is neutral.

To further understand the effects of such factors, a coordination number analysis for the permeating ions through OprP and OprO has been carried out. The average number of protein or water contacts within the specified cut-off distance from the permeating ion in the different regions of the pore is termed as coordination number (see an earlier study (18), for details regarding the calculation of the coordination number). Ion dehydration is one of the most important factors for the passage of ions through narrow pores (37) and can be the rate-limiting step in ion transport as reported for anion-selective channels (38–40). Removal of water molecules from ion hydration shells is an energetically unfavorable process that needs to be compensated by favorable protein contacts inside the pore. Considering all these factors, the coordination analysis can yield important insight concerning the interaction between the permeating ions, waters, the protein, and their interplay in the different regions of the pore. Such an analysis has also been exploited to decipher the K^+ selectivity of potassium channels (41–43).

Phosphate ions lose a maximum of only five water molecules in the central region of OprO, which are compensated by protein contacts (Fig. 3 *B*). The total number of contacts, i.e., the sum of water and protein contacts, remains almost constant throughout the length of the pore. By contrast, in OprP phosphate ions lose a maximum of seven water molecules. Compared with OprO, because of the small average diameter of OprP in the central region and also because of the smaller fluctuation in diameters (Fig. 2, *A* and *B*), more water molecules are stripped off from the phosphate ions while permeating through OprP and are replaced with more suitable—in terms of binding to a channel—protein contacts as coordinating ligands. This may contribute to the stronger binding of phosphate in OprP as compared with OprO.

In the case of diphosphate transport through OprO, diphosphate ions lose at maximum seven water molecules in the central region of the pore. These are compensated by an almost equivalent number of more favorable protein contacts (Fig. 3 *B*). This is also reflected in the PMF profiles by the presence of the two energetically favorable central binding sites, D1 and D2, in OprO (Fig. 3 *A*). The total number of contacts for diphosphate ions remains almost constant throughout the length of the OprO channel (Fig. 3 *B*). However, during the diphosphate transport through OprP more water molecules are stripped away, i.e., ten water molecules in OprP compared with seven in OprO (Fig. 3 *B*). But contrary to OprO, not all lost water contacts are compensated by favorable protein contacts as highlighted in Fig. 3 *B* (and Fig. 4 *B*) via the green circle. In this case the total number of contacts (water and protein) for diphosphate in OprP dropped significantly, from an average value of 19 contacts throughout the length of the channel to only 14 contacts when the diphosphate is close to binding site D2. As ion dehydration—which is energetically not favorable—is not completely compensated for by favorable protein contacts, this leads to an energetic penalty for diphosphate transport and in turn diminishes the affinity of binding site D2 for diphosphate in OprP.

Swapping the specificity of OprO and OprP

The PMF profiles for phosphate and diphosphate transport suggest important roles for two nonconserved residues between OprO and OprP that are located in the central region of the channels, namely D114 and F62 in OprO whereas the corresponding residues in OprP are Y114 and Y62 (Fig. 2 *B*). These residues are present in the close vicinity of the binding sites for phosphate and diphosphate ions in OprO and OprP and may be crucial in determining the specificity of the channels. It can be hypothesized that by swapping these two residues of OprP and OprO at these two particular positions, i.e., residue 62 and 114, that the phosphate specificity of OprP and the diphosphate specificity of OprO can be interchanged. To further understand the effects of these residues on the specificity of OprP and OprO, double mutants of each of the porins were generated in silico. Residues Y62 and Y114 of OprP were mutated to the corresponding residues of OprO, i.e., phenylalanine (F) and aspartate (D), respectively. We denote the double mutant Y62F/Y114D of OprP as the P→O mutant for the sake of clarity in our discussion. Conversely the double mutant F62Y/D114Y of OprO is denoted as the O→P mutant. The PMF profiles for the transport of phosphate and diphosphate through the P→O and the O→P mutants

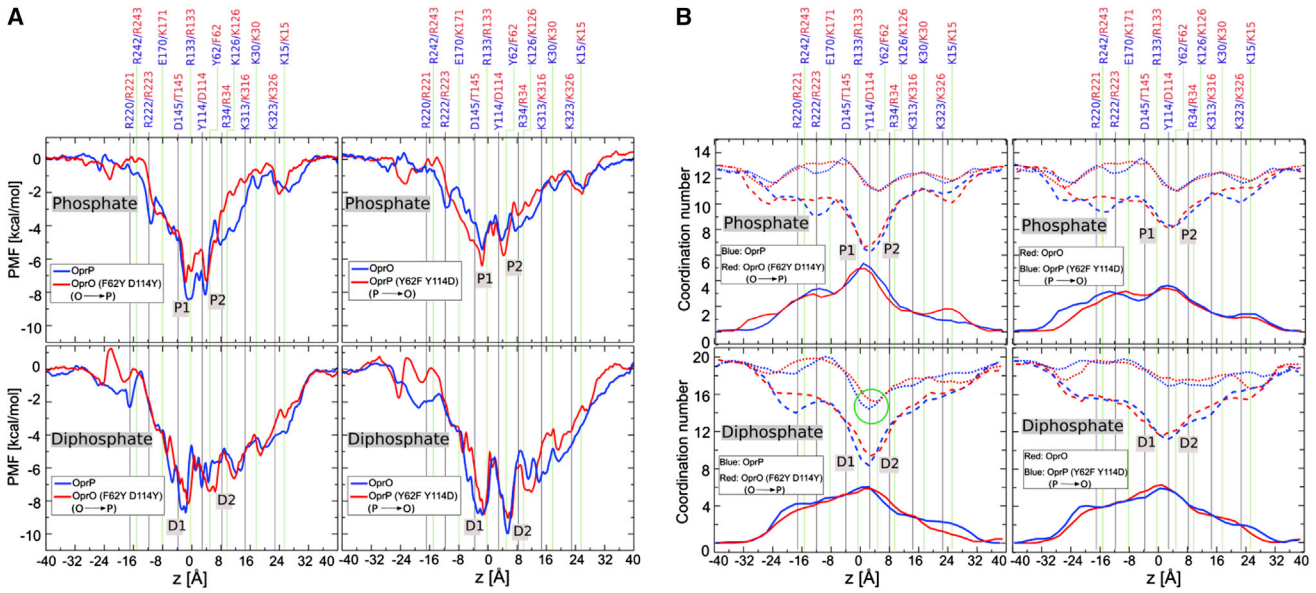

FIGURE 4 (*A*) PMF profiles for the permeation of phosphate and diphosphate ions through mutants of OprO and OprP, i.e., the OprO double mutant O→P (F62Y/D114Y) and the OprP double mutant P→O (Y62F/Y114D). For comparison the PMF profiles for wild-type OprO and OprP are also shown. Important residues of OprP and OprO along the ion permeation pathway are mapped onto the PMF profiles with respect to their positions along the *z* axis and labeled at the top of the figure: OprP (*blue labels*); and the corresponding residues in OprO (*red labels*). (*B*) Coordination numbers, i.e., protein (*solid line*), water (*dash line*), and total (*dotted line*) contacts for the permeation phosphate and diphosphate ions through mutants of OprO and OprP, i.e., the OprO double mutant O→P (F62Y/D114Y) and the OprP double mutant P→O (Y62F/Y114D). The coordination numbers for wild-type OprO and OprP are also shown for comparison. To see this figure in color, go online.

have been calculated and are compared with the wild-type OprP and OprO (Fig. 3 *A*).

The PMFs for phosphate permeation through the wild-type channels showed potential wells in OprP that are 2 kcal/mol deeper than in OprO. This likely leads to a stronger binding of phosphate in OprP compared with OprO and provides a possible reason for a phosphate specificity of OprP (Fig. 3 *A*). To swap the phosphate specificity of OprP and OprO using double mutant proteins, phosphate should have a stronger binding in the O→P mutant (F62Y/D114Y) of OprO compared with the P→O mutant (Y62F/Y114D) of OprP. Indeed the O→P mutant of OprO reveals a binding depth of 8 kcal/mol for phosphate whereas the P→O mutant of OprP has a binding depth of 6 kcal/mol for phosphate (Fig. 4 *A*). Hence the PMF profiles suggested that via double mutants, i.e., Y62F/Y114D of OprP and F62Y/D114Y of OprO, the phosphate specificity of OprP and OprO may be swapped.

The major difference that may cause the diphosphate specificity of OprO relative to OprP is the presence of the additional binding site D2 for diphosphate in OprO and the corresponding absence of the site D2 in OprP (Fig. 3 *A*). To swap the diphosphate specificity of the OprO and OprP double mutants, diphosphate should experience an additional binding site D2 in the P→O mutant (Y62F/Y114D) of OprP and the absence of the same site in the O→P mutant (F62Y/D114Y) of OprO. PMF profiles for the diphosphate permeation through double mutants reveal the presence of the site D2 in the P→O mutant of OprP (Fig. 4 *A*). The O→P mutant of OprO starts to lose the binding site D2 for diphosphate (Fig. 4 *A*). Hence with the suggested double mutants, the diphosphate specificity of OprP and OprO may be swapped. The corresponding coordination number profiles for both double mutants furthermore implies interchanged features of water-protein contacts for phosphate and diphosphate permeation (Fig. 4 *B*).

To further understand the changes in PMF profiles with the mutant channels, we calculated electrostatic potential maps of the wild-type OprP and OprO channels as well as their double mutants (Fig. 5). Such electrostatic potential maps, which essentially show the electrostatic interactions with the permeating ions, can play a key role in assigning specificities to a channel. For example, in the case of aquaporin channels, the substrate specificities between different subfamilies of aquaporins can be rationalized based only on the electrostatic profiles of the channels (44). The potential map for the wild-type OprP has a stronger electropositive region at the central region of the channel (indicated by *blue*) compared with the wild-type OprO (Fig. 5, *A* and *C*). This provides a possible hint for the stronger binding of phosphate in OprP compared with OprO. However, the O→P double mutant of OprO has a stronger electropositive region (Fig. 5 *D*) in the central region of the channel compared with the P→O double mutant of OprP (Fig. 5 *B*), providing a rationale for a stronger binding of phosphate ions to the O→P double mutant of OprO. In fact, the P→O double mutant of OprP of has an electrostatic potential map very

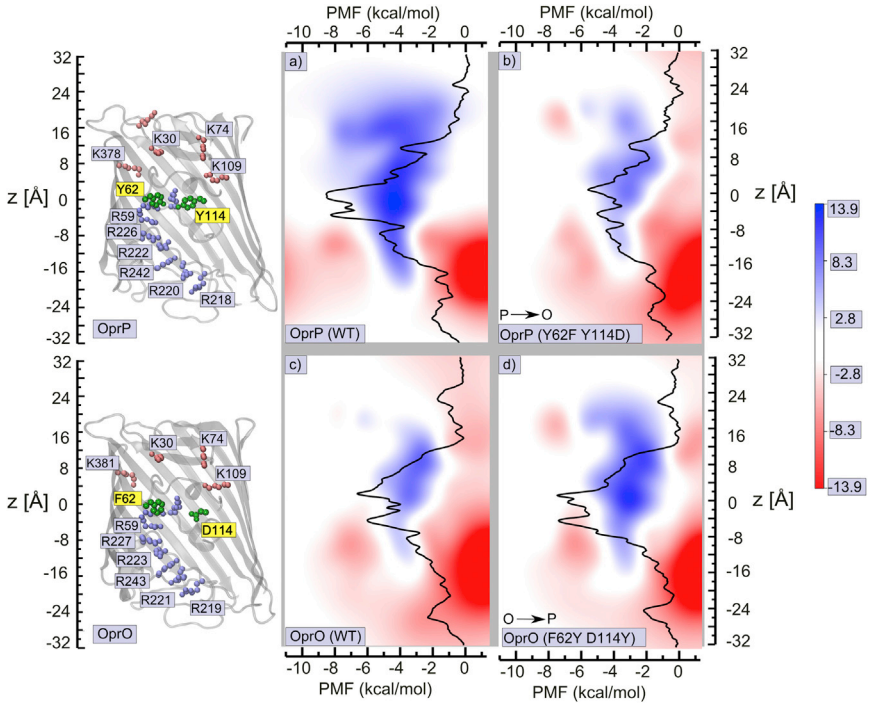

FIGURE 5 Electrostatic potential maps for (*a*) wild-type OprP, (*b*) P→O mutant (Y62F/Y114D) of OprP, (*c*) wild-type OprO, and (*d*) O→P mutant (F62Y/D114Y) of OprO. The OprP and OprO channels together with important residues are mapped along the potential maps to enable the identification of possible residues that are responsible for particular features of the potential maps. In addition, PMF profiles for the phosphate ion permeation through each of the channels are mapped onto the respective potential maps to show the correlation between the energetic of the phosphate transport and the electrostatic potential profiles. The potential maps are in the *y*-*z* plane at an *x* position corresponding to the middle of one of the three pores (see Fig. S2) and are generated using the PMEPlot plug-in for VMD (27,48). The potential maps are color-coded with the unit kcal/(mol*e) according to the scale shown at the right side of the figure. The potential maps are averaged over unbiased simulations of 25 ns time length each. To see this figure in color, go online.

similar to the wild-type OprO potential map (Fig. 5, *B* and *C*). Conversely, the O→P double mutant of OprO has an electrostatic potential map, particularly the strong electropositive region at the center of the channel, which is comparable with the potential map of the wild-type OprP (Fig. 5, *A* and *D*). The theoretical similarities of the O→P double mutant of OprO and OprP are confirmed by the crystal structure of the O→P double mutant, which shows that phosphate binds at an identical position compared with that in OprP (Fig. 1 *D*).

In addition to the phosphate and diphosphate binding specificity, we investigated the potassium chloride (KCl) conductance properties of the wild-type OprP and OprO channels as well as their mutants, utilizing applied field simulations (see Supporting Material for details). These simulations reveal an approximately two times higher conductance for the wild-type OprO compared with the wild-type OprP, which is in agreement with the electrophysiological experiments (Table S3). The P→O mutant (Y62F/Y114D) of OprP yielded a channel conductance for KCl similar to wild-type OprO (Table S3). By contrast, the O→P mutant (F62Y/D114Y) mutant of OprO did not switch to a conductance similar to OprP.

Inspired by the above results with computer simulations where we have shown that in silico mutants could swap the specificity for phosphate and diphosphate of OprP and OprO, we decided to experimentally test the mutants for their change in specificity. As the P→O mutant (Y62F/Y114D) of OprP has diphosphate specificity and a KCl conductance similar to OprO, we generated the P→O mutant (Y62F/Y114D) of OprP experimentally and investigated the mutant for its phosphate/diphosphate specificity using titration experiments to block chloride conductance with phosphate and diphosphate (see Table 1).

Previous electrophysiological bilayer measurements indicated that phosphate binds more strongly to OprP whereas diphosphate binds more strongly to OprO. These results were also found in this study, where previous experiments were repeated (see Table 1). Interestingly, the P→O mutant (Y62F Y114D) of OprP indeed displays a stronger binding for diphosphate compared with phosphate in bilayer measurements. Based on the experimental verification, we can conclude that the OprP (Y62F Y114D) mutant has become diphosphate selective and that by changing the two residues in the specificity filter region, it now behaves like OprO in terms of substrate specificity.

CONCLUSIONS

We have determined the high-resolution x-ray crystal structure of OprO to enable the structural investigations to decode the diphosphate specificity of OprO compared with the phosphate specificity of the homologous channel OprP. Free-energy MD simulations provided the molecular basis for the difference in the specificity of OprO and OprP. Based on the details gained from the modeling study, we have shown that in silico mutations in the binding site region can swap the phosphate specificity of OprP and the diphosphate specificity of OprO. These findings were experimentally validated by the fact that the OprP double mutant (Y62F/Y114D) is specific for diphosphate specificity in bilayer measurements. The outcomes in this study provide

a molecular basis to understand the substrate specificity of two structurally highly similar OM channels, as well as to engineer the substrate specificity properties of these channels. These findings can be exploited to change or to fine-tune the specificity of different channels and porins. Furthermore, understanding the permeation properties of OM channels is of utmost importance for antibiotics research because the improvement of translocation of these drugs into the bacteria is one of the challenging problems in the field (45,46).

ACCESSION NUMBERS

Coordinates and structure factors for wild-type OprO and the double mutant F62Y/D114Y have been deposited in the Protein Data Bank with accession codes 4RJW and 4RJX respectively.

SUPPORTING MATERIAL

Supporting Materials and Methods, two figures, and four tables are available at http://www.biophysj.org/biophysj/supplemental/S0006-3495(15)00770-5.

AUTHOR CONTRIBUTIONS

R.B., B.v.d.B., and U.K. designed research; N.M. and U.K. performed and analyzed MD simulations; S.G., I.B.-U., and R.B. performed and analyzed electrophysiology experiments; B.v.d.B. performed x-ray crystallography and analyzed data; and N.M., R.B., B.v.d.B., and U.K. wrote the article.

ACKNOWLEDGMENTS

The research leading to these results has received support from the Innovative Medicines Initiatives Joint Undertaking under Grant Agreement No. 115525, resources that are composed of financial contributions from the European Union's seventh framework programme (FP7/2007-2013) and European Federation of Pharmaceutical Industries and Associations companies in-kind contribution. Furthermore, we acknowledge funding from ITN-2014-607694-Translocation. We also thank Prof. R.E.W. Hancock for helpful discussions and the personnel of the National Synchrotron Light Source (NSLS) beamline X6A and the Diamond Light Source (DLS) beamline i02 for beamtime and beamline support. In addition we acknowledge Dr. Arnaud Basle for expert direction of the Newcastle Structural Laboratory.

REFERENCES

1. Benz, R. 2006. Bacterial and Eukaryotic Porins: Structure, Function, Mechanism. John Wiley & Sons, Hoboken, NJ.
2. Nikaido, H. 2003. Molecular basis of bacterial outer membrane permeability revisited. *Microbiol. Mol. Biol. Rev.* 67:593–656.
3. Benz, R., A. Schmid, and G. H. Vos-Scheperkeuter. 1987. Mechanism of sugar transport through the sugar-specific LamB channel of *Escherichia coli* outer membrane. *J. Membr. Biol.* 100:21–29.
4. Schülein, K., K. Schmid, and R. Benzl. 1991. The sugar-specific outer membrane channel ScrY contains functional characteristics of general diffusion pores and substrate-specific porins. *Mol. Microbiol.* 5:2233–2241.
5. Maier, C., E. Bremer, …, R. Benz. 1988. Pore-forming activity of the Tsx protein from the outer membrane of *Escherichia coli*. Demonstration of a nucleoside-specific binding site. *J. Biol. Chem.* 263:2493–2499.
6. Benz, R., and R. E. W. Hancock. 1987. Mechanism of ion transport through the anion-selective channel of the *Pseudomonas aeruginosa* outer membrane. *J. Gen. Physiol.* 89:275–295.
7. Hancock, R. E. W., K. Poole, and R. Benz. 1982. Outer membrane protein P of *Pseudomonas aeruginosa*: regulation by phosphate deficiency and formation of small anion-specific channels in lipid bilayer membranes. *J. Bacteriol.* 150:730–738.
8. Aksimentiev, A. 2010. Deciphering ionic current signatures of DNA transport through a nanopore. *Nanoscale.* 2:468–483.
9. Howorka, S., and Z. Siwy. 2009. Nanopore analytics: sensing of single molecules. *Chem. Soc. Rev.* 38:2360–2384.
10. Modi, N., M. Winterhalter, and U. Kleinekathöfer. 2012. Computational modeling of ion transport through nanopores. *Nanoscale.* 4:6166–6180.
11. Nestorovich, E. M., C. Danelon, …, S. M. Bezrukov. 2002. Designed to penetrate: time-resolved interaction of single antibiotic molecules with bacterial pores. *Proc. Natl. Acad. Sci. USA.* 99:9789–9794.
12. Pagès, J. M., C. E. James, and M. Winterhalter. 2008. The porin and the permeating antibiotic: a selective diffusion barrier in Gram-negative bacteria. *Nat. Rev. Microbiol.* 6:893–903.
13. Moraes, T. F., M. Bains, …, N. C. Strynadka. 2007. An arginine ladder in OprP mediates phosphate-specific transfer across the outer membrane. *Nat. Struct. Mol. Biol.* 14:85–87.
14. Benz, R., C. Egli, and R. E. W. Hancock. 1993. Anion transport through the phosphate-specific OprP-channel of the *Pseudomonas aeruginosa* outer membrane: effects of phosphate, di- and tribasic anions and of negatively-charged lipids. *Biochim. Biophys. Acta.* 1149:224–230.
15. Hancock, R. E. W., and R. Benz. 1986. Demonstration and chemical modification of a specific phosphate binding site in the phosphate-starvation-inducible outer membrane porin protein P of *Pseudomonas aeruginosa*. *Biochim. Biophys. Acta.* 860:699–707.
16. Modi, N., I. Barcena-Uribarri, …, U. Kleinekathöfer. 2015. Tuning the affinity of anion binding sites in porin channels with negatively charged residues: molecular details for OprP. *ACS Chem. Biol.* 10:441–451.
17. Modi, N., I. Bárcena-Uribarri, …, U. Kleinekathöfer. 2013. Role of the central arginine R133 toward the ion selectivity of the phosphate specific channel OprP: effects of charge and solvation. *Biochemistry.* 52:5522–5532.
18. Modi, N., R. Benz, …, U. Kleinekathöfer. 2012. Modeling the ion selectivity of the phosphate specific channel OprP. *J. Phys. Chem. Lett.* 3:3639–3645.
19. Pongprayoon, P., O. Beckstein, …, M. S. Sansom. 2009. Simulations of anion transport through OprP reveal the molecular basis for high affinity and selectivity for phosphate. *Proc. Natl. Acad. Sci. USA.* 106:21614–21618.
20. Hancock, R. E. W., C. Egli, …, R. J. Siehnel. 1992. Overexpression in *Escherichia coli* and functional analysis of a novel PPi-selective porin, oprO, from *Pseudomonas aeruginosa*. *J. Bacteriol.* 174:471–476.
21. Siehnel, R. J., C. Egli, and R. E. W. Hancock. 1992. Polyphosphate-selective porin OprO of *Pseudomonas aeruginosa*: expression, purification and sequence. *Mol. Microbiol.* 6:2319–2326.
22. Sukhan, A., and R. E. W. Hancock. 1995. Insertion mutagenesis of the *Pseudomonas aeruginosa* phosphate-specific porin OprP. *J. Bacteriol.* 177:4914–4920.
23. van der Ley, P., H. Amesz, …, B. Lugtenberg. 1985. Monoclonal antibodies directed against the cell-surface-exposed part of PhoE pore protein of the *Escherichia coli* K-12 outer membrane. *Eur. J. Biochem.* 147:401–407.
24. Kabsch, W. 2010. XDS. *Acta Crystallogr. D Biol. Crystallogr.* 66:125–132.

25. McCoy, A. J., R. W. Grosse-Kunstleve, …, R. J. Read. 2005. Likelihood-enhanced fast translation functions. *Acta Crystallogr. D Biol. Crystallogr.* 61:458–464.

26. Afonine, P. V., R. W. Grosse-Kunstleve, …, P. D. Adams. 2012. Towards automated crystallographic structure refinement with phenix.refine. *Acta Crystallogr. D Biol. Crystallogr.* 68:352–367.

27. Humphrey, W., A. Dalke, and K. Schulten. 1996. VMD: visual molecular dynamics. *J. Mol. Graph.* 14:33–38.

28. Phillips, J. C., R. Braun, …, K. Schulten. 2005. Scalable molecular dynamics with NAMD. *J. Comput. Chem.* 26:1781–1802.

29. MacKerell, A. D., D. Bashford, …, M. Karplus. 1998. All-atom empirical potential for molecular modeling and dynamics studies of proteins. *J. Phys. Chem. B.* 102:3586–3616.

30. Kleinekathöfer, U., B. Isralewitz, …, K. Schulten. 2011. Domain motion of individual F1-ATPase β-subunits during unbiased molecular dynamics simulations. *J. Phys. Chem. A.* 115:7267–7274.

31. Vanommeslaeghe, K., and A. D. MacKerell, Jr. 2012. Automation of the CHARMM general force field (CGenFF) I: bond perception and atom typing. *J. Chem. Inf. Model.* 52:3144–3154.

32. Vanommeslaeghe, K., E. P. Raman, and A. D. MacKerell, Jr. 2012. Automation of the CHARMM general force field (CGenFF) II: assignment of bonded parameters and partial atomic charges. *J. Chem. Inf. Model.* 52:3155–3168.

33. Darden, T., D. York, and L. Pedersen. 1993. Particle mesh Ewald: an $N\cdot\log(N)$ method for Ewald sums in large systems. *J. Chem. Phys.* 98:10089–10092.

34. Tuckerman, M., B. J. Berne, and G. J. Martyna. 1992. Reversible multiple time scale molecular dynamics. *J. Chem. Phys.* 97:1990–2001.

35. Darve, E., and A. Pohorille. 2001. Calculating free energies using average force. *J. Chem. Phys.* 115:9169–9183.

36. Hénin, J., and C. Chipot. 2004. Overcoming free energy barriers using unconstrained molecular dynamics simulations. *J. Chem. Phys.* 121: 2904–2914.

37. Richards, L. A., A. I. Schäfer, …, B. Corry. 2012. The importance of dehydration in determining ion transport in narrow pores. *Small.* 8:1701–1709.

38. Bormann, J., O. P. Hamill, and B. Sakmann. 1987. Mechanism of anion permeation through channels gated by glycine and gamma-aminobutyric acid in mouse cultured spinal neurones. *J. Physiol.* 385:243–286.

39. Linsdell, P., and J. W. Hanrahan. 1998. Adenosine triphosphate-dependent asymmetry of anion permeation in the cystic fibrosis transmembrane conductance regulator chloride channel. *J. Gen. Physiol.* 111: 601–614.

40. Verdon, B., J. P. Winpenny, …, M. A. Gray. 1995. Volume-activated chloride currents in pancreatic duct cells. *J. Membr. Biol.* 147:173–183.

41. Egwolf, B., and B. Roux. 2010. Ion selectivity of the KcsA channel: a perspective from multi-ion free energy landscapes. *J. Mol. Biol.* 401:831–842.

42. Fowler, P. W., K. Tai, and M. S. Sansom. 2008. The selectivity of K+ ion channels: testing the hypotheses. *Biophys. J.* 95:5062–5072.

43. Thomas, M., D. Jayatilaka, and B. Corry. 2007. The predominant role of coordination number in potassium channel selectivity. *Biophys. J.* 93:2635–2643.

44. Oliva, R., G. Calamita, …, M. Pellegrini-Calace. 2010. Electrostatics of aquaporin and aquaglyceroporin channels correlates with their transport selectivity. *Proc. Natl. Acad. Sci. USA.* 107:4135–4140.

45. Ceccarelli, M., and P. Ruggerone. 2008. Physical insights into permeation of and resistance to antibiotics in bacteria. *Curr. Drug Targets.* 9:779–788.

46. Singh, P. R., M. Ceccarelli, …, K. R. Mahendran. 2012. Antibiotic permeation across the OmpF channel: modulation of the affinity site in the presence of magnesium. *J. Phys. Chem. B.* 116:4433–4438.

47. Smart, O. S., J. G. Neduvelil, …, M. S. Sansom. 1996. HOLE: a program for the analysis of the pore dimensions of ion channel structural models. *J. Mol. Graph.* 14:354–360.

48. Aksimentiev, A., and K. Schulten. 2005. Imaging alpha-hemolysin with molecular dynamics: ionic conductance, osmotic permeability, and the electrostatic potential map. *Biophys. J.* 88:3745–3761.